# How to measure the thickness of a lubrication film in a pancake bubble with a single snapshot?

Omer Atasi, Benoit Haut, Sam Dehaeck, Adrien Dewandre, Dominique Legendre, Benoit Scheid

# How to measure the thickness of a lubrication film in a pancake bubble with a single snapshot?

O. Atasi,[1,2] B. Haut,[1] S. Dehaeck,[1] A. Dewandre,[1] D. Legendre,[2] and B. Scheid[1,a)]
[1]*Transfers, Interfaces and Processes (TIPs), Université libre de Bruxelles, 50 Avenue F.D. Roosevelt, 1050 Brussels, Belgium*
[2]*Institut de Mécanique des Fluides de Toulouse (IMFT), CNRS, Université de Toulouse, 2 Allée du Pr Camille Soula, 31400 Toulouse, France*

In the in-line bright-field image of a pancake-like bubble, a ring-shaped zone of maximum intensity is visible, called the glare ring. It is due to multiple interactions of light with the bubble interface. In this study, we develop a method to measure the thickness of the lubrication film around a pancake-like bubble translating inside a microchannel, based on the location of this glare ring. By means of ray tracing, a correlation is proposed to relate the film thickness to the location of the glare ring with respect to the bubble edge and to the ratio of refractive indices of the inner and outer phases. This makes the method also applicable to inviscid pancake drops. Additionally, for static bubbles, the method can be used to measure the depth of a microchannel. For moving bubbles, pro-vided the speed of the bubble is also measured, the method can be used to measure surface tension or viscosity. Finally, the method can also be extended to viscous drops, provided the shape function of the interface is adapted.

Large air bubbles translating inside confined geometries, referred to as pancake bubbles, are encountered in countless situations including oil extraction, gas-liquid absorption or treatment of pulmonary disorders. The dynamics of these bubbles depends on the thickness of the lubrication film in-between the bubble and the walls of the channel in which they translate. Direct measurement methods of this film thickness usually require interferometric top-view imaging[1,2] or bright-field side-view imaging.[3] Indirect measurement methods rely instead on a model that relates another measured quantity to the film thickness itself. The most classical indirect method consists of measuring the bubble velocity and recovering the film thickness via a Bretherton-like model.[4–6] This *classical method* requires a temporal sequence of images and the knowledge of the channel height as well as of the fluid properties, such as the viscosity and the surface tension. We propose in this work a method, also indirect, that only requires a single instantaneous bright-field image of the bubble and the sole knowledge of the refractive indices of the fluids.

Numerous methods based on bright-field images allow one to characterize the geometrical properties of bubbles or drops. For example, a ray tracing technique has been used to relate the optical pattern viewed on bright-field images of layered bubbles to the geometry of these layers.[7] The method proposed in this work relies on the location of specific intensity peaks, called glare points, created on the image of a bubble illuminated using a light beam (e.g., emitted from a laser or diffusive light source).[8] These intensity peaks correspond to different interaction orders of the beam with the bubble. When two of these intensity peaks are visible on the bright-field image of a spherical bubble, the distance between these two points can be used to obtain the bubble diameter. This method is called glare point velocimetry and sizing (GPVS)[9] and has been used to size particles or measure the refractive index of liquids. In GPVS, the glare points are visualized in focus. When these glare points are visualized out of focus, interference patterns form on the image. The period of these interference fringes can be used to size particles in suspensions or sprays.[10,11] This method is called Interferometric Laser Imaging for Droplet Sizing (ILIDS). In contrast to the above methods, we use in this paper an in-line configuration. In this case, the glare points connect to form a glare ring or circle, as described by Dehaeck and van Beeck.[12] Even though in-line measurements of these glare points have been used to size bubbles[12] and measure refractive indices,[13] as far as we are aware, they have never been used to measure the thickness of lubrication films.

The method we propose requires an in-line bright-field image of a bubble translating in a microchannel, as illustrated in Fig. 1 and shown in the left of Fig. 2. The microchannel, of width $w$ and height $2a$, is illuminated with a collimated light source from the top of the scene and an in-line observation is performed from the bottom with a

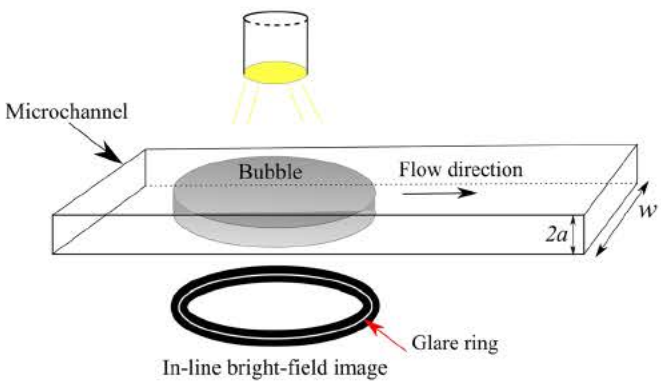


FIG. 1. Schematic of the optical setup.

a)bscheid@ulb.ac.be

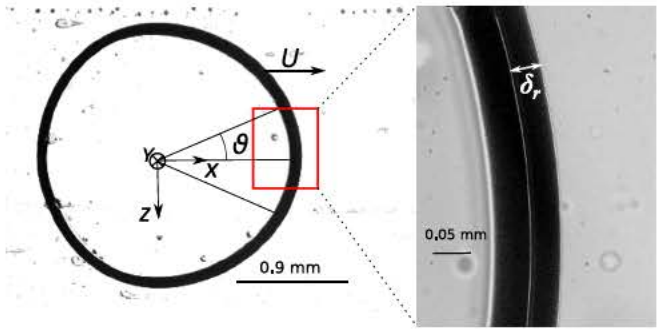


FIG. 2. (Left) In line bright field image of a pancake bubble inside a micro channel. (Right) Zoom on view of the glare ring inside the shadow region, the contrast of which has been enhanced for visualization purposes.

standard transmission microscope. A side-view of the optical setup is shown in Fig. 3. The rays producing the glare ring on the bright-field image are refracted on the bubble-liquid interface, reflected and refracted a second time before exiting the bubble from the bottom of the scene. The ray that exits the microchannel perpendicularly is depicted in red in Fig. 3. The distance between the position at which this ray exits the bubble and the bubble edge is denoted as $\delta_r$ (see Figs. 2 and 3). As inferred from Fig. 3, $\delta_r$ can be correlated with the thickness of the lubrication film, $h_\infty$, provided the instantaneous shape of the bubble in a frame moving at the speed $U$ of the bubble can be determined through a model.

For this purpose, we define a Cartesian coordinate system $(x, y, z)$, as represented in Figs. 2 and 3. For the sake of simplicity, the bubble shape function $F(x, y)$ is considered on the plane $z=0$. Furthermore, by symmetry about the axis $y=a$, only the bottom half of the shape is considered. As sketched in Fig. 3, this shape is composed of a dynamic meniscus of thickness $h(x)$ connecting the flat lubrication

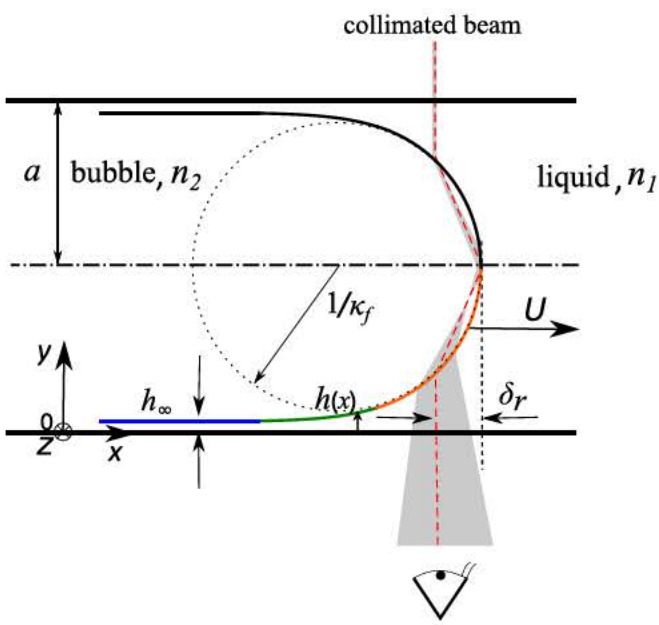


FIG. 3. Side view of a pancake bubble inside a microchannel of half height $a$. The bubble translates with a velocity $U$ and generates on the walls a lubri cation film of constant thickness, $h_\infty$. The static meniscus (orange line) of constant radius $1/\kappa_f$ is connected to the lubrication film (blue line) through a dynamic meniscus (green line). The light rays (in gray) producing the glare ring on the bright field image have been reconstructed by ray tracing, $n_1$ and $n_2$ being the refractive indices of each phase. The ray that exits the channel perpendicularly (red dashed line) is used to determine $\delta_r$.

film of thickness $h_\infty$ and the static meniscus of constant curvature $\kappa_f$ at the front of the bubble. In the frame of the lubrication approximation, i.e., for $h_\infty/a \ll 1$, and provided that $a \ll w$, $h(x)$ can be obtained by solving the following Bretherton equation balancing the capillary and viscous forces:[14]

$$h^3\kappa' = 3U\frac{\mu}{\sigma}(h - h_\infty), \tag{1}$$

where the prime denotes the $x$-derivative, $\kappa$ is the surface curvature, $\mu$ is the viscosity of the liquid, and $\sigma$ is the surface tension of the bubble/liquid interface. In virtue of the least degeneracy principle,[15] the full expression of the curvature $\kappa = h''(1+h'^2)^{3/2}$ is used to patch the curvatures between the dynamic and static menisci. Balestra *et al.*[16] performed 2D numerical simulations of the Stokes equation and established a correlation for the curvature of the static meniscus

$$a\kappa_f = \frac{1 + 2.925\left(U\frac{\mu}{\sigma}\right)^{2/3}}{1 + 0.495\left(U\frac{\mu}{\sigma}\right)^{2/3}}, \tag{2}$$

as well as for the thickness of the lubrication film

$$\bar{h}_\infty(U) \equiv \frac{h_\infty}{a} = \frac{1.337\left(U\frac{\mu}{\sigma}\right)^{2/3}}{1 + 1.337 \times 2.19\left(U\frac{\mu}{\sigma}\right)^{2/3}}. \tag{3}$$

The model of Balestra and the correlations (2) and (3) have been proven to be valid for $U\mu/\sigma \lesssim 5 \times 10^{-2}$.[16] Now, given a certain value of $U\mu/\sigma$, Eq. (1) is solved as an initial value problem, with $h(0) = h_\infty + \epsilon$, $h'(0) = h''(0) = \epsilon$, using $\epsilon = 10^{-3}$ and Eq. (3) to calculate $h_\infty$. The equation is solved until a patch of curvatures is reached [i.e., when $\kappa = \kappa_f$, with $\kappa_f$ calculated using Eq. (2)].

The corresponding bubble shape $F(x, y)$ is then reconstructed and implemented in a ray tracing algorithm that is detailed in the supplementary material. In short, the ray entering and exiting the system perpendicularly is calculated from the laws of reflection/refraction. From this, $\delta_r/a$ can be found for a given value of the refractive index ratio $m = n_1/n_2$ (see Fig. 3). Even though for gases $n_2 \approx 1$, the use of $m$ makes the method also applicable to inviscid pancake drops, as will be discussed later. The procedure is repeated for various values of $U\mu/\sigma$ and $m$ and the data points relating $\delta_r/a$ to $h_\infty/a$ are plotted in Fig. 4. It is observed that $\delta_r$ is linearly correlated to $h_\infty$, as shown by the best linear fits (dashed and solid lines in Fig. 4). Additionally, the value $\delta_{r,0}$ for $h_\infty = 0$ (empty symbols in Fig. 4) has been obtained by the analytical expression

$$a(\delta_{r,0}) = \frac{\delta_{r,0}}{1 - \frac{1+\sqrt{1+8m^2}}{4m^2}} \equiv \frac{\delta_{r,0}}{\xi(m)}, \tag{4}$$

following Dehaeck and van Beeck[12] in the case of a quiescent bubble for which the shape function reduces to half a

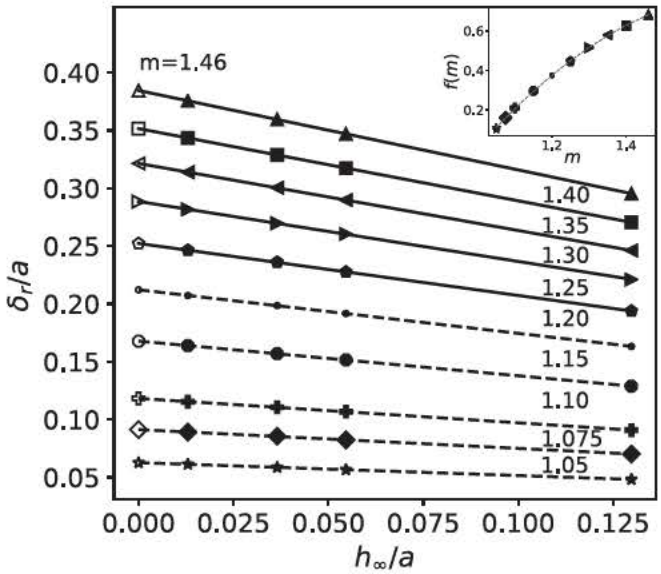


FIG. 4. Position of the glare ring relative to the bubble edge, $\delta_r/a$, as a function of the lubrication film thickness, $h_\infty/a$ for various values of the ratio of refractive indices $m$. Full symbols give values of $\delta_r/a$ computed with our ray tracing algorithm and empty symbols are calculated with Eq. (4). Lines for usual values of $m$ corresponding to bubbles (resp., drops) are solid (resp., dashed). The inset depicts the value of the function $f(m)$ appearing in Eq. (5) and its best second order polynomial fit (green dashed line).

circle of radius $a$. Finally, a correlation based on the data of Fig. 4 can be written as

$$\bar{h}_\infty(\delta_r) \equiv \frac{h_\infty}{a(\delta_{r,0})} = \frac{\xi(m)}{f(m)}\left(1 - \frac{\delta_r}{\delta_{r,0}}\right), \tag{5}$$

where $f(m) = Am^2 + Bm + C$ with $A = -1.41 \pm 0.05$, $B = 4.9 \pm 0.2$, and $C = -3.5 \pm 0.1$ being the best fitted coefficients together with their standard deviations (see the inset of Fig. 4). Note that this correlation is established using only perpendicular rays (see the dashed red line in Fig. 3). For finite acceptance angles of the acquisition system (see the gray area in Fig. 3), corrections based on the numerical aperture (NA) of the objective are derived in the supplementary material. For the configuration used here with NA = 0.3, it leads to a bias of about 3% in $\delta_r$ or $a(\delta_r)$, which is comparable to their experimental determination uncertainties. Nevertheless, for the calculation of $\bar{h}_\infty(\delta_r)$, this error cancels out as can be inferred from Eq. (5) and Fig. S3 of the supplementary material.

At this stage, the two correlations (3) and (5) can be used independently for the indirect measurement of the lubrication film thickness, $h_\infty$. In the following, they are referred to as the *Classical* and *Present* methods, respectively. Experiments are performed at room temperature using mineral and silicon oils as working liquids. Air bubbles are produced inside a microchannel filled with these liquids, hence $m = n_1$. It is worth noting that the two methods do not require the same set of input parameters as summarized in Table I, in which the parameter values obtained using appropriate instruments are provided. For instance, $a$ is an input parameter for the classical method and has been measured with a 3D confocal microscope over a wide area of the channel. Contrarily, $a$ is an output parameter for the present method and has been obtained by measuring $\delta_{r,0}$ at one (or several) specific $(x, z)$ location for a quiescent bubble. Yet, the two measurements of the channel depth are in excellent agreement. Next, a constant pressure difference is applied along the channel to induce the translation of bubbles. Images such as the one shown on the right of Fig. 2 are used to measure $\delta_r$. During these experiments, the bubble translation velocity, $U$, is also measured by tracking the nose of the bubble on consecutive images (such as the one shown on the left of Fig. 2). Consequently, the two methods can directly be compared, as plotted in Fig. 5. The excellent agreement with the parity line thus validates the approach.

TABLE I. Summary of the indirect measurement of $\bar{h}_\infty$ $h_\infty/a$ with the classical and present methods. The measurement techniques and the corresponding instruments used for the input parameters are (a) rheometer (Rheosens), (b) tensiometer (KRUSS DSA 100), (c) 3D confocal microscope (Keyence VK X 200), (d) bright field microscope (Nikon eclipse Ti 5), (e) standard camera (ALLIED GC2540), and (f) refractometer (ATAGO DR A1). The lines corresponding to the output parameters are in bold face.

| Method | Parameters | Mineral oil | Silicon oil | Technique |
|---|---|---|---|---|
| *Classical* | $\mu$ [mPa/s] | 22 ± 0.5 | 19 ± 0.5 | (a) |
| | $\sigma$ [mN/m] | 29.8 ±0.1 | 20.6 ± 0.1 | (b) |
| | $a$ [$\mu$m] | 109 ± 3.1 | | (c) |
| | $U$ [$\mu$m/s] | $U \pm \Delta U$ | | (d), (e) |
| | $\bar{h}_\infty(U)$ | see Fig. 5 | | Eq. (3) |
| *Present* | $m$ | 1.4638 | 1.402 | (f) |
| | $\delta_r$ [$\mu$m] | $\delta_r \pm \Delta\delta_r$ | | (d), (e) |
| | $\boldsymbol{a(\delta_{r,0})}$ **[$\mu$m]** | **110±1.5** | **111.5±0.2** | Eq. (4) |
| | $\bar{h}_\infty(\delta_r)$ | see Fig. 5 | | Eq. (5) |

Furthermore, by equating Eqs. (5) and (3), the present method can be used to measure the velocity $U$ of the bubble, provided the ratio $\sigma/\mu$ is added to the set of input parameters. As the present method necessitates only a single snapshot of the bubble, it can be advantageous when the velocity of the bubble is not constant or when a high speed camera is not available. More interestingly, if $U$ and $\delta_r$ are measured simultaneously, combining the methods enables one to measure the ratio $\sigma/\mu$, referred to as the visco-capillary velocity. Nevertheless, as it can be observed in Fig. 5, the uncertainties associated with the calculation of $\bar{h}_\infty(\delta_r)$ are smaller for

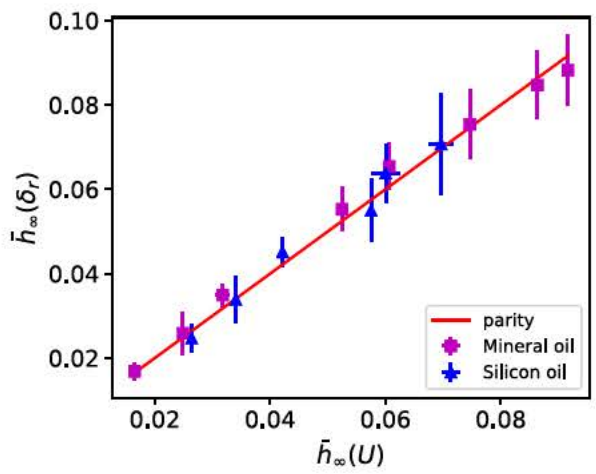


FIG. 5. Comparison of indirect measurements of the lubrication film thickness $\bar{h}_\infty$ $h_\infty/a$, between the classical method using Eq. (3) and the present method using Eq. (5).

TABLE II. Measured values of the visco capillary velocity using direct techniques as given in Table I and (in bold) the indirect method that combines the classical and present methods.

| | Mineral oil | Silicon oil | |
|---|---|---|---|
| $\frac{\sigma}{\mu}$ [m/s] | 1.35 ± 0.03 | 1.08 ± 0.03 | see Table I |
| | **1.26±0.26** | **1.08±0.09** | Eqs. (3) (5) |

lower values of this variable due to slight blurring of the images at higher translation velocities. For this reason, the precision on the calculation of $\sigma/\mu$ is better for small values of $\bar{h}_\infty(\delta_r)$, and here, only the data points corresponding to a translation velocity lower than 0.007 m/s have been kept for validation purpose. The results are again in excellent agreement with independent techniques as shown in Table II.

Note that to increase the accuracy on $\delta_r$, we have used the value averaged over the range of angles $\vartheta \approx \pm 15°$, as represented on the right of Fig. 2. Despite the fact that the shape function $F(x, y)$ used in this work is strictly valid for $\vartheta = 0$, the corresponding variation made on the shape for small variations along the perimeter of the bubble remains small. Indeed, using the model of Burgess and Foster,[17] we have estimated the maximum of the variation $\Delta h_\infty/a$ at $\pm 0.004$, i.e., well below the uncertainty of our experimental measurements, as it can be deduced from the amplitude of the error bars in Fig. 5.

Now, our method can easily be adapted to other situations such as a pancake drop instead of a pancake bubble, at the sole condition that $m > 1$. To this purpose, the new shape function should be constructed depending additionally on the viscosity ratio, denoted $\lambda = \mu_d/\mu$, between the viscosity of the drop, $\mu_d$, and the one of the surrounding liquid.[16] Updating the ray tracing algorithm with these new shapes should allow one to extend the correlating function in Eq. (5) for non-zero viscosity ratio, i.e., $f(m, \lambda)$. Nevertheless, as mentioned earlier, the correlating function $f(m)$ is already valid for inviscid pancake droplets. Practically, Balestra *et al.*[16] have demonstrated that the shape of droplets for $\lambda \lesssim 10^{-2}$ is almost identical to the shape obtained for $\lambda = 0$, as it has been considered in this work. This said, it is worth mentioning that the ratio of refractive indices $m$ being lower for droplets than for bubbles, the sensitivity of the method would also be lower, as inferred from Fig. 4 by comparing the slopes of the solid and dashed lines.

In conclusion, we have shown how one can measure the lubrication film thickness around a pancake bubble or an inviscid drop, from a single bright-field image, as can be typically obtained with a transmission microscope. We also demonstrated how one can combine this technique with the measurement of the bubble velocity to extract a measure of the visco-capillary velocity. It is believed that the method presented in this work can be of wide use in the future as it requires a standard microscope and a visual inspection of a single image, hence a smaller amount of less sophisticated instruments, as summarized in Table I.

See supplementary material for a detailed description of the ray tracing procedure.

O.A. and B.S. thank the F.R.S-FNRS for financial support and Innoviris (RBC) through the project Microeco. O.A. also thanks the "Fonds Alice et David van Buuren" and "Jaumotte-Demoulin" Foundation.

[1]H. Chen, Q. Meng, and J. Li, Appl. Phys. Lett. **107**, 141608 (2015).
[2]A. Huerre, O. Theodoly, A. M. Leshansky, M. P. Valignat, I. Cantat, and M. C. Jullien, Phys. Rev. Lett. **115**, 064501 (2015).
[3]O. Atasi, S. Khodaparast, B. Scheid, and H. A. Stone, Phys. Rev. Fluids **2**, 094304 (2017).
[4]M. J. F. Warnier, E. V. Rebrov, M. H. J. M. de Croon, V. Hessel, and J. C. Schouten, Chem. Eng. J. **135**, S153 (2008).
[5]J. A. Howard, P. A. Walsh, and E. J. Walsh, Int. J. Heat Mass Transfer **54**, 4752 (2011).
[6]S. Khodaparast, O. Atasi, A. Deblais, B. Scheid, and H. A. Stone, Langmuir **34**, 1363 (2018).
[7]A. van der Net, L. Blondel, A. Saugey, and W. Drenckhan, Colloids Surf., A **309**, 159 (2007).
[8]H. C. Hulst and R. T. Wang, Appl. Opt. **30**, 4755 (1991).
[9]S. Dehaeck, J. P. A. J. v. Beeck, and M. L. Riethmuller, Exp. Fluids **39**, 407 (2005).
[10]G. Kœnig, K. Anders, and A. Frohn, J. Aerosol Sci. **17**, 157 (1986).
[11]A. R. Glover, S. M. Skippon, and R. D. Boyle, Appl. Opt. **34**, 8409 (1995).
[12]S. Dehaeck and J. van Beeck, Appl. Opt. **46**, 5957 (2007).
[13]M. R. Gavrilovic, Eur. Phys. J. D **71**, 316 (2017).
[14]F. P. Bretherton, J. Fluid Mech. **10**, 166 (1961).
[15]M. Van Dyke, *Perturbation Methods in Fluid Mechanics* (Academic Press, 1964).
[16]G. Balestra, L. Zhu, and F. Gallaire, Microfluid. Nanofluid. **22**, 67 (2018).
[17]D. Burgess and M. R. Foster, Phys. Fluids A **2**, 1105 (1990).